Comparison between calculations with the AMD code and experimental data for peripheral collisions of ^{93}Nb + ^{93}Nb, ^{116}Sn at 38 MeV/nucleon

S. Piantelli,[1,*] A. Olmi,[1] P. R. Maurenzig,[1,2] A. Ono,[3] M. Bini,[1,2] G. Casini,[1] G. Pasquali,[1,2] A. Mangiarotti,[4] G. Poggi,[1,2]
A. A. Stefanini,[1,2] S. Barlini,[1,2] A. Camaiani,[1,2] C. Ciampi,[1,2] C. Frosin,[1,2] P. Ottanelli,[1,2] and S. Valdré[1]
[1]*INFN Sezione di Firenze, I-50019 Sesto Fiorentino, Italy*
[2]*Dipartimento di Fisica, Universitá di Firenze, I-50019 Sesto Fiorentino, Italy*
[3]*Department of Physics, Tohoku University, Sendai 980-8578, Japan*
[4]*Instituto de Física da Universidade de São Paulo, 05508-090 São Paulo, Brazil*

(Received 7 February 2019; revised manuscript received 18 April 2019; published 21 June 2019)

Experimental data concerning binary events in peripheral collisions for the systems ^{93}Nb + ^{93}Nb and ^{93}Nb + ^{116}Sn at 38 MeV/nucleon, collected with the FIASCO setup, are compared with calculations performed with the dynamic code AMD, coupled with the statistical code GEMINI used as an afterburner. The comparison focuses on the properties of the quasiprojectile (QP) and on the total multiplicities of the emitted light charged particles. A good reproduction of the average mass ratio, charge Z, and center-of-mass angle of the QP is obtained in the examined impact parameter range ($b \approx$ 7–12 fm). Concerning the light charged particles, a general agreement is found for the total emitted charge, while some discrepancy remains for the multiplicities of the various species, especially for the protons, which are always overestimated by the calculations.

DOI: 10.1103/PhysRevC.99.064616

I. INTRODUCTION

Heavy ion collisions in the Fermi energy domain (20–50 MeV/nucleon) represent a transition regime, where the mean field plays an important role (like at low energies), but the nucleon-nucleon collisions become more and more relevant in determining the dynamics. As such, heavy ion reactions at Fermi energies represent a challenge for theoretical models, because they display a variety of phenomena strongly dependent on the impact parameter. In fact, in peripheral and semiperipheral reactions the cross section is dominated by binary exit channels, with the production of two main fragments, the quasiprojectile (QP) and the quasitarget (QT); they may be accompanied by a significant contribution of midvelocity emissions [1–10]. At the other extreme, multifragmentation phenomena represent a very important reaction channel for central collisions [11–15].

Transport models are an important tool to describe these reactions and they are able to account for many aspects, although a unified description suitable for the whole impact parameter range, from central to peripheral collisions, is difficult. Such models can be divided into two main classes. In one class there are the models based on the BUU (Boltzmann-Uehling-Uhlenbeck) approach, which follow the evolution in time of the phase space density: e.g., among many others, the stochastic meanfield (SMF) [16] and the Boltzmann-Langevin one body (BLOB) [17]. In the other class there are the models that follow the evolution of the nucleon coordinates and momenta, namely the various flavors of quantum molecular dynamics (QMD) models. Very recently Zhang *et al.* [18] performed a very extensive theoretical comparison of different models, belonging to classes of both BUU and QMD type, focusing on the most critical ingredient of the transport equations, namely the collision term. In another recent paper by Xu *et al.* [19], a comparison of several different models of the two classes was performed by simulating the same collision, namely ^{197}Au + ^{197}Au, at 100 and 400 MeV/nucleon, with a fixed impact parameter of $b = 7$ fm. In particular, the rapidity distribution and the collective flow were compared, finding a considerable spread in the outcome of the different models. As a consequence it is particularly useful to compare the predictions of the models with experimental data, in order to establish more stringent constraints.

Among the various QMD models, we consider here the AMD (antisymmetrized molecular dynamics [20]), which is able to give a good description of the main characteristics of heavy ion reactions at Fermi energies. In the literature one can find some comparisons of AMD calculations and experimental data, but they are mainly focused on central collisions (see, e.g., [21,22]) or based on inclusive data [23]. For example in Ref. [23] it was shown that some properties (like angular distributions, energy spectra, and production cross section) of intermediate mass fragments (IMFs) observed in inclusive measurements for the system ^{12}C + ^{12}C at 95 MeV/nucleon are well reproduced by AMD followed by GEMINI++ [24] as an afterburner.

In this paper the focus is on the QP properties and on the light charged particles (LCPs) produced in peripheral and semiperipheral heavy ion collisions for the systems ^{93}Nb + ^{93}Nb and ^{93}Nb + ^{116}Sn at 38 MeV/nucleon. It will be shown that for these systems the AMD model, coupled with GEMINI [24–26], is well suited to describe the average characteristics

---

[*] Corresponding author: piantelli@fi.infn.it

of the projectile remnants in binary collisions, from about 50% to 100% of the grazing impact parameter.

The experimental data used here have already been the subject of other papers [10,27–29] that were mainly focused on the properties of LCPs and IMFs. On the basis of the results published therein, it will be shown that not only the QP properties but also the experimental total particle multiplicities in peripheral and semiperipheral binary collisions are reasonably well reproduced by the calculations, with the possible exception of protons, which appear to be somewhat overestimated.

II. EXPERIMENTAL SETUP

The experimental data were collected with the FIASCO setup, which is described in detail elsewhere [30]. Here only the main characteristics are briefly recalled. The FIASCO setup consisted of different types of detectors. There was a shell of 24 position sensitive parallel plate avalanche detectors (PPADs) to measure the velocity vectors of heavy ($Z > 9$) fragments with high efficiency [30] and low energy thresholds ($\sim$0.1 MeV/nucleon), so that they were able to detect also the low-energy QT. The angular coverage was about 70% of the forward hemisphere, from 0.2° up to about 90°. In the polar range 0.5°–6°, behind the six most forward PPADs, 96 ΔE-E silicon telescopes (with a thickness of 200 μm for the first layer and of 500 μm for the second one) were devoted to the measurement of charge and energy of the QP. Therefore, when the QP was detected in coincidence by a PPAD and a silicon telescope behind it, it was possible to obtain also the mass of the QP by means of the information on its energy and time of flight. The setup was completed by 182 three-layer phoswich telescopes, covering about 30% of the forward hemisphere, aimed at identifying the mass of LCPs (p, d, t, and α) and the charge of heavier fragments (in the range $Z = 1$ to ≈ 26) and measuring their times of flight.

III. AMD MODEL

The AMD model is described in detail elsewhere [20,22,31,32], so only the main features are briefly recalled here. AMD is a transport model which describes the time evolution of a system of nucleons, by depicting the state of the system at each time step as a Slater determinant of Gaussian wave packets. The time evolution is achieved by applying the time-dependent variational principle, thus obtaining an equation of motion governed by a Hamiltonian that describes the mean field contribution by means of an effective interaction. Such an interaction is based, in the present case, on the Skyrme-force parametrization SLy4 of [33] with a soft symmetry energy (slope parameter $L = 46$ MeV), while the normal density term, S_0, has the standard value of 32 MeV [22]. A stiff symmetry energy ($L = 108$ MeV) can be obtained by changing the density dependent term in the SLy4 force [32]. Unless otherwise stated, the stiff symmetry energy is used in this paper.

In the present work, we employ a new method for two-nucleon collisions based on the test particles which are randomly generated at every time step. The test particles are the samples taken from the exact one-body Wigner function defined for the AMD wave function of antisymmetrized Gaussian wave packets. See Appendix C of Ref. [32] for the method to generate test particles. The attempt of a collision between two test particles is judged by a geometrical condition as in many other transport codes (see, e.g., Ref. [18]). A possible benefit of this new method is that the collisions will reflect the exact density distribution, in contrast to the previous method that employs the so-called physical coordinates [34], which can represent the phase-space distribution only approximately. In the new method, when it is decided that two test particles $(\boldsymbol{r}_1, \boldsymbol{p}_1)$ and $(\boldsymbol{r}_2, \boldsymbol{p}_2)$ collide, a collision is still performed by changing the momenta of the two physical coordinates $(\boldsymbol{R}_{k_1}, \boldsymbol{P}_{k_1})$ and $(\boldsymbol{R}_{k_2}, \boldsymbol{P}_{k_2})$ that are associated with the two colliding test particles. The final momenta $\boldsymbol{P}'_k$ ($k = k_1, k_2$) are allowed by the Pauli principle when $\nu|\boldsymbol{R}_k - \boldsymbol{R}_j|^2 + |\boldsymbol{P}'_k - \boldsymbol{P}_j|^2/(4\hbar^2\nu) < 1.46^2$ is satisfied for all j ($\neq k$) with the same spin-isospin state as k. Here ν is the width parameter with the usual value of 0.16 fm^{-2} [32,35]. The existence of the backward transformation from the physical coordinates to the variables of an AMD wave function is also required [34]. The transition probability depends on the *in-medium* nucleon-nucleon cross section, which can be considered, within some limits, as a free parameter of the model. In the version of the code used in this work, the parametrization introduced in Ref. [36] was adopted, namely

$$\sigma = \sigma_0 \tanh(\sigma_{\text{free}}/\sigma_0), \quad \text{with} \quad \sigma_0 = y\,\rho^{-2/3} \tag{1}$$

where ρ is the nuclear density and y a screening parameter. With the value $y = 0.85$ proposed in Ref. [36], the parameter for the Pauli blocking (1.46), together with other parameters explained below for momentum fluctuations and for cluster correlations, have been chosen so as to approximately reproduce the fragment charge distribution in the central Xe + Sn collisions at 50 and 32 MeV/nucleon and to have the degree of stopping $R = 0.55$ at 50 MeV/nucleon and $R = 0.62$ at 32 MeV/nucleon which may be compared to the experimental data in Ref. [37]. The calculated stopping variable is defined for the transverse and longitudinal kinetic-energy components, $E_i^{\perp}$ and $E_i^{\parallel}$, in the center-of-mass (c.m.) frame by $R = (\sum_i E_i^{\perp})/(2\sum_i E_i^{\parallel})$, where the summation is for all the light charged particles and heavier fragments produced in all the calculated central events. In the present work, the study of the dependence on the in-medium cross section is extended to peripheral collisions at Fermi energies by testing two values of y (0.85 and 0.42) corresponding to different reductions of the in-medium cross section.

When a two-nucleon collision has occurred and the physical coordinates have been updated to $\boldsymbol{P}'_{k_1}$ and $\boldsymbol{P}'_{k_2}$, we may virtually consider a similar scattering of the two test particles to the final momenta $\boldsymbol{p}'_1$ and $\boldsymbol{p}'_2$, which contain physical fluctuations. In the present work, we turned on an option to incorporate these fluctuations into the dynamics. When a wave packet k is emitted at a later time, the fluctuation $\Delta\boldsymbol{p}'_k$ of its most recent collision is added to the momentum of the nucleon k. This is a simplified way of introducing wave packet splitting, and it should influence the energy spectra of emitted particles. The energy and momentum conservation

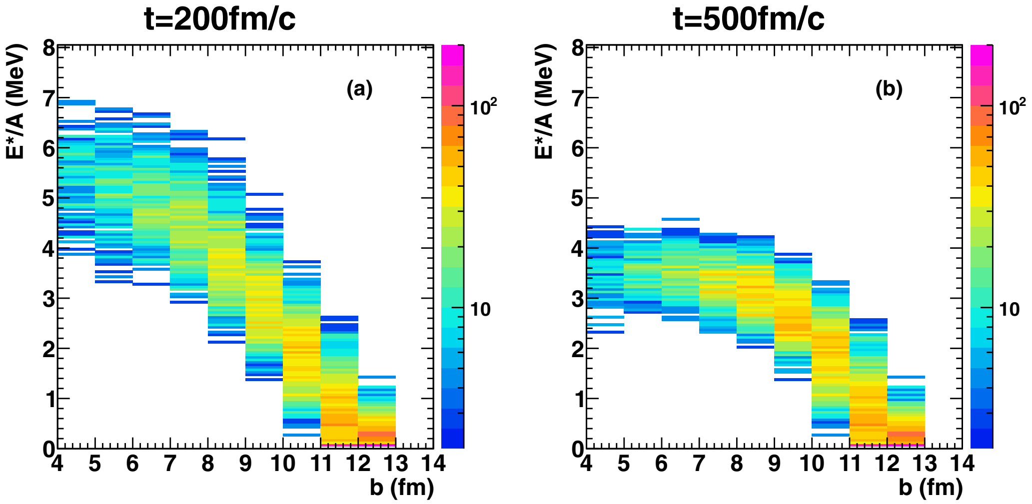

FIG. 1. Two-dimensional correlation of $E^\star/A$ vs b for the system ^{93}Nb + ^{93}Nb obtained from AMD (with $y = 0.85$) at $t = 200$ fm/c (a) and 500 fm/c (b).

laws are taken into account in a way similar to that in Ref. [35]. When a cluster is emitted, the sum of the fluctuations $\Delta \boldsymbol{p}'_k$ of its nucleons is added to the c.m. motion of the cluster.

The cluster correlations are explicitly taken into account by allowing each of the scattered nucleons to form a light cluster such as a deuteron, triton, or α particle. The method is the same as that employed in Refs. [23,32], except that a new method is adopted in the present work to suppress the cluster correlation in nuclear medium. The probability of attaching a nucleon i to one of the scattered nucleons k (or a subcluster k) is reduced by multiplying a factor $1 - 0.3f$, where f is an approximate Wigner function, with the contribution from i excluded, at the phase-space point of the center of mass of i and k. The method of binding several clusters to form light nuclei (Li, Be, etc.) is almost the same as that of Ref. [23]. However, we here choose a stricter condition for binding than in Ref. [23] so that the chance of binding several clusters is reduced. The necessary conditions for a pair of clusters to be linked now include that their relative kinetic energy should satisfy $\frac{1}{2}\mu V_{\rm rel}^2 < 10$ MeV and that each of them is one of the three closest clusters of the other. For the energy conservation, we adjust the relative momentum of the bound light nucleus and the third cluster that has the minimum value of a measure $(r + 7.5\ \text{fm})(1.2 - \cos\theta)/\min(\epsilon_\parallel,\ 5\ \text{MeV})$, as in Ref. [23]. However, this measure is divided by a factor 2 in the present work for a candidate cluster that is in a light nucleus already bound at a former time, and thus light nuclei are favored as the third cluster for the energy conservation.

The time evolution of the AMD calculation was usually stopped at a time (from now on called "switching time" and indicated as $t_{\rm sw}$) of 500 fm/c, which was verified to be a reasonable time to assume that the dynamics of the collision has already established the final partitions. Many tests were done also stopping the AMD calculation at values of $t_{\rm sw}$ from 200 up to 10 000 fm/c to verify a possible dependence of the obtained results on the choice of the switching time. In this paper, each AMD calculation usually consisted of 7000 or more events, except for the case with $t_{\rm sw} = 10\,000$ fm/c where only 2500 events were generated, due to the extremely long computation time. The impact parameters were distributed in a triangular shape between 0 and 13 fm, a value that is slightly larger than the grazing impact parameter of the collisions (about 12.3 and 12.6 fm for ^{93}Nb + ^{93}Nb and ^{93}Nb + ^{116}Sn, respectively).

The primary fragments produced by AMD are rather excited, so that it is necessary to let them decay before comparing the calculated results with the experimental data. Therefore, 100 secondary events were generated for each AMD event by means of a statistical afterburner. The masses and charges of the fragments produced by a single AMD event, as well as their excitation energies and angular momenta, are the input parameters for the following afterburner. For each replica of the same AMD event, the reaction plane was axially rotated at random, in a coherent way for all the reaction products.

The excitation energy of the QP was calculated as $E^\star = \langle H\rangle + B_{gs}$. Here $\langle H\rangle$ is the expectation value of the Hamiltonian calculated for the internal wave function of the QP,[1] while B_{gs} is the binding energy of the QP in its ground state [38]. The behavior of the excitation energy per nucleon, $E^\star/A$, of the QP as a function of the impact parameter is presented in panels (a) and (b) of Fig. 1 for AMD calculations with $y = 0.85$ at times of 200 and 500 fm/c, respectively. Starting from grazing collisions, $E^\star/A$ first increases with decreasing impact parameter for both times. At 200 fm/c, $E^\star/A$ steadily increases until it reaches a value of about 5 MeV/nucleon around 5 fm and then it tends to flatten. At 500 fm/c, initially there is a similar slope, but then below 8 fm the correlation levels off at a value of $E^\star/A$ around 3.5 MeV/nucleon,

---

[1] The QP (like any other fragment) was identified by linking together wave packets located at a distance less than 5 fm.

because the excited nuclei cool down, losing both mass and excitation energy.

In this paper the statistical code GEMINI was used as an afterburner, both in its Fortran90 [25] and C++ version [24] with the standard parameters [39]. In fact the results of the two versions of the statistical code present some differences, which are found to be appreciable for the multiplicities of the emitted LCPs. In the following, for brevity, the two versions of GEMINI will be referred to as GEM90 and GEM++, respectively.

The so produced secondary events were then filtered with a software replica of the experimental setup, keeping into account both the geometrical coverage and the detection thresholds of the PPADs. Concerning the LCPs and IMFs, no filtering was performed because their multiplicities were compared with the published data of Ref. [10], which had already been corrected for the geometrical coverage of the phoswich telescopes.[2] The experimental effects can be appreciated from the comparison of the filtered events with those produced directly by the calculations, which will be shortly called "4π events" in the following.

One point to be noted is that, while the AMD calculation takes into proper account the mutual Coulomb repulsion of all the reaction products, GEMINI makes each product decay on its own, without further acceleration. This means that when using short values of t_{sw}, the final secondary fragments will lack the full Coulomb reacceleration and their velocity vectors will not have the proper asymptotic values. This affects both the emission angles and kinetic energies, which are therefore expected to be somewhat too low. For example, for $t_{\mathrm{sw}} = 200$ (500) fm/c the total kinetic energy in the c.m. frame of two Nb-like fragments will be low by about 45 (20) MeV with respect to the asymptotic value of fully accelerated fragments, corresponding to a kinetic energy deficit of about 2.5% (1.1%) for quasielastic events. This minor effect has been taken into account by applying a small multiplicative correction to the C_b scale (see next section) before comparing calculations performed with different values of the switching-time parameter.

IV. RESULTS

A. Event sorting

Peripheral and semiperipheral collisions have been experimentally selected by requiring that only two heavy fragments ($Z > 9$) are detected in the PPADs. The selection of binary events was implemented by rejecting those events that severely violate the binary kinematics, based on the relative angle α between the c.m. velocities of the two detected fragments [acceptance condition: $\cos(\alpha) \leqslant -0.8$] and on the difference between their azimuthal angles (acceptance condition: $|\varphi_{\mathrm{QP}} - \varphi_{\mathrm{QT}}| = 180^\circ \pm 20^\circ$). This selection will be referred to as "collinearity condition" in the following. Of the two heavy fragments, the forward-emitted one (in the c.m. frame) is assumed to be the QP, the other the QT. The same selections are applied to the calculated events.

Since the impact parameter is not accessible to experiments, it is necessary to find another observable that allows a fair comparison between calculated and experimental events as a function of the centrality of the collision. In the present case we introduce the variable C_b defined as

$$C_b = \tfrac{1}{2}\, M\, v_{\mathrm{QP}}^{\mathrm{cm}}\, v_{\mathrm{QT}}^{\mathrm{cm}}, \qquad (2)$$

where $v_{\mathrm{QP(QT)}}^{\mathrm{cm}}$ is the secondary velocity of the QP (QT) in the c.m. reference frame and M is the total mass of the system. The relationship of C_b with the more common TKE (total kinetic energy) will be explained later in this section.

The correlation between C_b and the impact parameter b was studied by means of the events produced by AMD plus GEMINI and is shown in Fig. 2. Panels (a) and (d) display the two-dimensional correlations b vs C_b (in 4π) for the systems $^{93}\mathrm{Nb} + {}^{93}\mathrm{Nb}$ and $^{93}\mathrm{Nb} + {}^{116}\mathrm{Sn}$, respectively. For a more quantitative analysis, the average impact parameter $\langle b \rangle$ and the standard deviation of the b distribution are shown as a function of C_b in panels (b) and (c), respectively, for both reactions. Panels (e) and (f) show the same information the other way around, namely the mean $\langle C_b \rangle$ and the standard deviation of the C_b distribution, respectively, this time as a function of b. Full symbols refer to calculations for binary events in 4π. Full circles are for the systems $^{93}\mathrm{Nb} + {}^{93}\mathrm{Nb}$ [black for a value $y = 0.85$ of the screening parameter defined in Eq. (1) and green for $y = 0.42$] and full squares refer to the system $^{93}\mathrm{Nb} + {}^{116}\mathrm{Sn}$ ($y = 0.42$). From panels (b) and (e), one observes that there is a good average correlation between C_b and b, from grazing collisions down to $C_b \approx 500$ MeV, or to $b \approx 5$ fm, and that the sensitivity to the screening parameter y is negligible. Panels (c) and (f) show also that the width of the correlation becomes increasingly wide with increasing centrality and below $C_b \approx 1000$ MeV the estimate of b has an uncertainty of the order of ± 1 fm or greater. In the same figure, the open symbols show the negligible effect of the experimental filter, which requires that there be only two *detected* fragments with $Z > 9$ and that they must additionally satisfy the "collinearity condition." This latter request helps rejecting ternary (or higher multiplicity) events that *appear* to be binary just because only two fragments passed the experimental filter.

In a previous paper [10], we correlated the impact parameter b with another observable, TKEL (total kinetic energy loss), obtained with a kinematic coincidence method (KCM [40]). As shown in Fig. 15 of Ref. [10], such a correlation was determined with two methods that gave similar results: (i) by direct integration of the experimental cross section from grazing collisions downwards, and (ii) by means of a transport code based on molecular dynamics [41]. By definition, TKEL = E_{cm} − TKE, where $E_{\mathrm{cm}} = \mu \epsilon_{\mathrm{beam}}$ is the c.m. kinetic energy in the entrance channel[3] (μ is the reduced mass and ϵ_{beam} the energy-per-nucleon of the beam) and TKE is the c.m. total kinetic energy of QP and QT.

---

[2] The reliability of the correction can be appreciated from Fig. 1 of [27], where the total charge in the forward c.m. hemisphere comes close to 41 (the charge of the projectile), with a small average deficit of about half a charge unit.

[3] $E_{\mathrm{cm}} = 1767$ (1930) MeV for $^{93}\mathrm{Nb} + {}^{93}\mathrm{Nb}$ ($^{116}\mathrm{Sn}$) at 38A MeV.

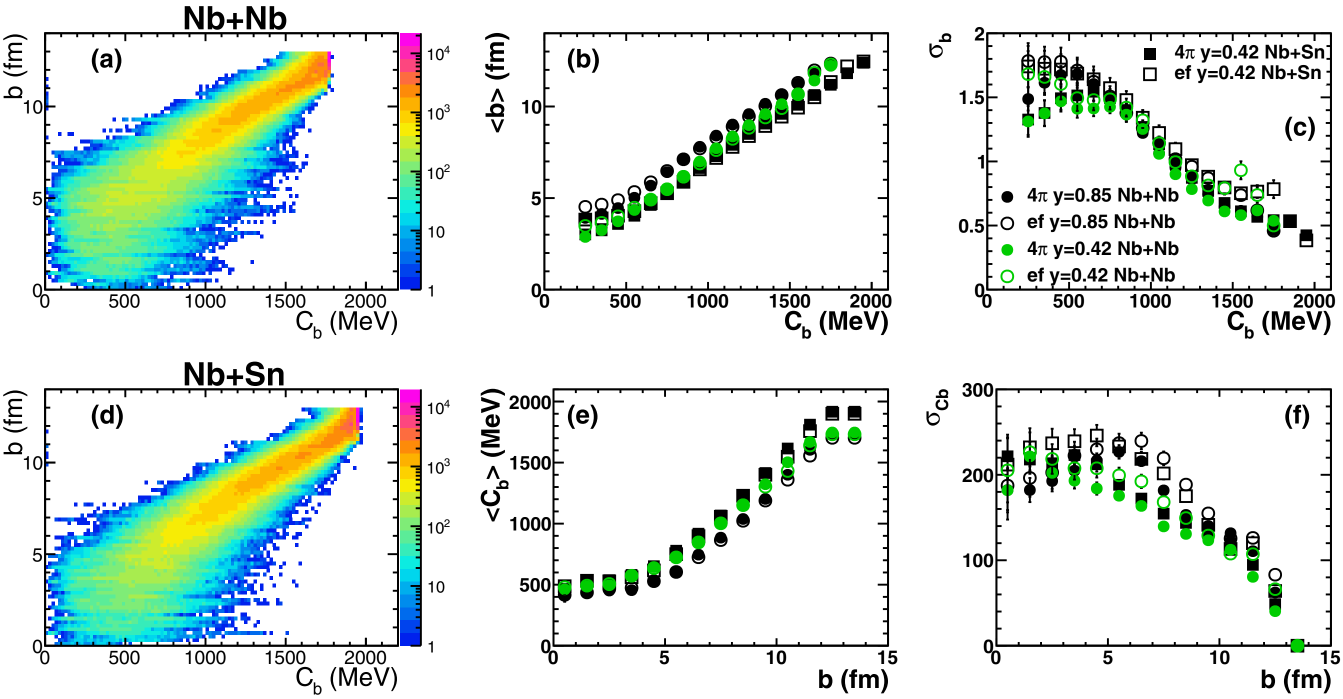

FIG. 2. Results of AMD plus GEM++ calculations, with $t_{\mathrm{sw}} = 500$ fm/c. Two-dimensional correlations b vs C_b for 4π data of (a) ^{93}Nb + ^{93}Nb (screening parameter $y = 0.85$) and (d) ^{93}Nb + ^{116}Sn ($y = 0.42$); (b) mean values and (c) standard deviations of the b distribution as a function of C_b; (e) mean values and (f) standard deviations of the C_b distribution as a function of b. Full and open symbols are for 4π and filtered results, respectively. Circles refer to ^{93}Nb + ^{93}Nb (black for $y = 0.85$ and green for $y = 0.42$) and squares to ^{93}Nb + ^{116}Sn.

Within classical kinematics and in the ideal case of a true binary collision with both C_b and TKE built from the c.m. primary velocities (i.e., before statistical de-excitation), these two quantities would exactly coincide. In the present case, we prefer to analyze and classify both the experimental and the calculated quasibinary events in terms of C_b, because it involves only the secondary velocities, which are experimentally available quantities. For the LCP multiplicities, the experimental data are taken from Ref. [10] and, for the sake of comparison with the calculations, also those experimental data will be presented in terms of C_b, assuming that – at least for (semi)peripheral collisions – C_b can be estimated from TKEL by means of the conversion $C_b \approx \mathrm{TKE} = E_{\mathrm{CM}} - \mathrm{TKEL}$.

The comparison will be restricted to the range $C_b >$ 700 MeV, one of the reasons (possibly the main one) being that, below this value, three-body events are quite abundant in the experiment and rather scarce in the calculations. As a consequence, any comparison both of the QP properties and of the LCP multiplicities below $C_b = 700$ MeV might become increasingly unreliable.

B. QP properties

A commonly used way to present the gross features of binary collisions at low and intermediate energies is by means of the so-called "diffusion plot" (i.e., the correlation between TKE and the mass of the QP) and "Wilczynski plot" (i.e., the correlation between TKE and the c.m. polar angle of the QP $\vartheta_{\mathrm{QP}}^{\mathrm{cm}}$). In previous papers [42,43] concerning data collected with a similar setup but at lower beam energies, the primary (or pre-evaporative) mass of the QP and its primary c.m. polar angle were estimated by means of the KCM. Since the kinematic method is based on the assumption of a binary reaction (with primary masses of QP and QT adding up to the total mass of the system), this procedure of estimating primary quantities loses its validity at Fermi energies when other reaction channels, such as the midvelocity emissions, become important.[4]

Due to these drawbacks, it is better to rely on directly measured quantities. The FIASCO setup measured the secondary velocity of the QP, but this does not allow one to obtain the QP secondary mass, except for the small number of events in which the QP was detected in coincidence by one PPAD and a Si telescope behind it [30]. However, using the secondary c.m. velocities of QP and QT, one can build the ratio

$$R_v = \frac{v_{\mathrm{QT}}^{\mathrm{cm}}}{v_{\mathrm{QP}}^{\mathrm{cm}} + v_{\mathrm{QT}}^{\mathrm{cm}}}, \tag{3}$$

which was used in Ref. [29] as an estimator of the ratio between the QP primary mass at separation and the sum of the primary masses of QP and QT,

$$R_A = \frac{A_{\mathrm{QP}}}{A_{\mathrm{QP}} + A_{\mathrm{QT}}}, \tag{4}$$

as far as the reaction can be considered binary.

---

[4] However, it was shown in Ref. [10] that TKEL can still be used as an estimator of the centrality of the collision.

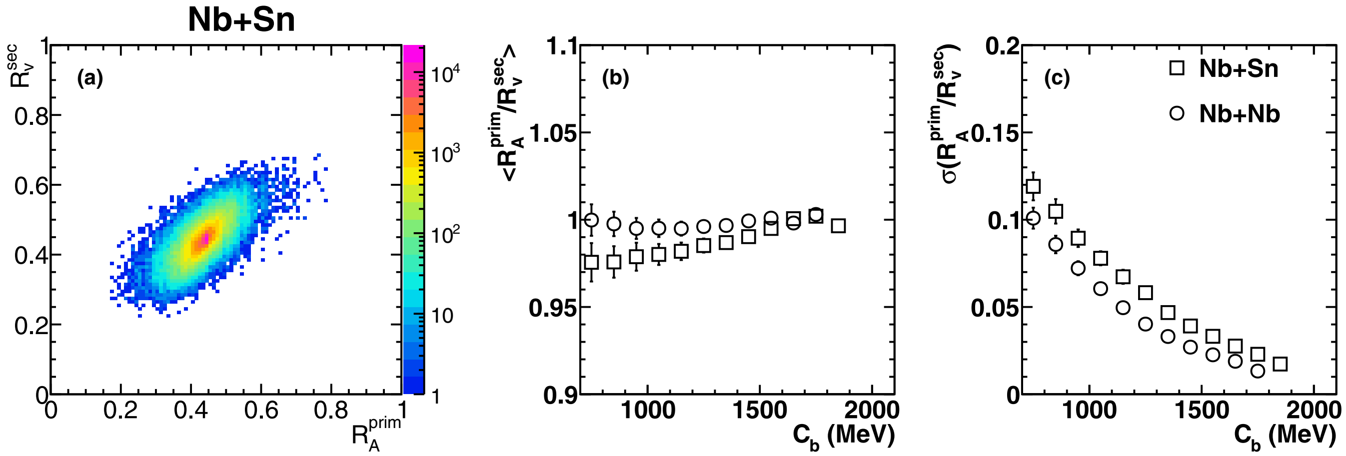

FIG. 3. Results of AMD plus GEM++ calculations, with $t_{sw} = 200$ fm/c: (a) two-dimensional distribution of R_v vs R_A for semiperipheral binary events with $C_b > 700$ MeV, in the system ^{93}Nb + ^{116}Sn ($y = 0.42$) at 38 MeV/nucleon (events filtered with the efficiency of the experimental setup); (b) average ratio $\langle R_A/R_v\rangle$ as a function of C_b, for both reactions ^{93}Nb + ^{93}Nb (circles) and ^{93}Nb + ^{116}Sn (squares); (c) standard deviation of the distribution of R_A/R_v as a function of C_b.

A check of this assumption is presented in Fig. 3 using the events produced by the AMD plus GEM++ calculation. Panel (a) shows the correlation between R_v (calculated with secondary velocities, i.e., after the afterburner) and R_A (calculated with the masses produced by AMD before applying the afterburner) for $C_b > 700$ MeV in the asymmetric system ^{93}Nb + ^{116}Sn. The switching time is $t_{sw} = 200$ fm/c, to be sure that the masses of QP and QT are close to the primary values they had at separation. The events, which are filtered with a software replica of the setup, satisfy the collinearity condition and are binary at both the primary and secondary level. The figure shows a clear correlation, peaked around 0.445 (the mass ratio of the colliding system) for both variables.

To be more quantitative, Fig. 3 presents, again as a function of C_b, also (b) the average ratio $\langle R_A/R_v\rangle$ and (c) its standard deviation, for both reactions ^{93}Nb + ^{93}Nb (circles) and ^{93}Nb + ^{116}Sn (squares). In both cases, the ratio $\langle R_A/R_v\rangle$ stays very close to 1 at all values of C_b. While this fact is just a trivial consequence of the system symmetry in ^{93}Nb + ^{93}Nb, it is not so for the asymmetric collision ^{93}Nb + ^{116}Sn. There one observes that the ratio starts at about 1 for very peripheral collisions and decreases with increasing centrality. However, the deviation from 1 is small ($\lesssim 2\%$), so that $R_v \approx R_A$ appears as a good approximation. Within the model, one can check the origin of this decrease. It is found that $\langle R_v\rangle$ remains close to 0.445 for all values of C_b and independently of the chosen value of t_{sw}. In contrast, if the quantity $\langle R_A\rangle$ of Eq. (4) is built with the masses delivered by AMD at t_{sw}, this mass ratio deviates from the entrance value (0.445) towards lower values, and this deviation increases with increasing t_{sw}. This fact suggests that while the masses of QP and QT become lighter and lighter, the total mass of the particles they emit is not proportional to their initial mass. Therefore, besides being the only one experimentally available, $\langle R_v\rangle$ appears to be a rather good estimator of the true primary masses at separation. The standard deviation of R_A/R_v has a similar behavior in both reactions: it is very narrow in peripheral collisions and then monotonically widens with increasing centrality.

At this point one can build a kind of diffusion plot for binary events both for the experimental data and for the calculated results. The two-dimensional correlations of $(100R_v)$ vs C_b produced by the calculation are shown in Figs. 4(a) and 4(d) for filtered events from the reactions ^{93}Nb + ^{93}Nb and ^{93}Nb + ^{116}Sn, respectively. A quantitative comparison with the experimental data of both systems is shown in the remaining panels of Fig. 4 for a few of the several calculations that were performed. Panels (b) and (e) show, as a function of C_b, the average quantity $\langle R_v\rangle$ and panels (c) and (f) the standard deviation of the R_v distribution. Full (red) squares represent the experimental data; the other symbols refer to calculations with $t_{sw} = 500$ fm/c, $y = 0.85$ (0.42) and GEM90 (GEM++) afterburner for the system Nb+Nb (Nb+Sn). Circles are for filtered results, asterisks for unfiltered ones.

In the experimental data for ^{93}Nb + ^{93}Nb, $\langle R_v\rangle$ is substantially constant as a function of C_b and close to 0.50 (as expected for a symmetric system), while in the asymmetric reaction it is close to 0.445 (the projectile-to-total mass ratio). Below $C_b \approx 1000$ MeV the experimental R_v shows a moderate (and unexplained) increasing trend in ^{93}Nb + ^{93}Nb. This effect is much more evident in the asymmetric ^{93}Nb + ^{116}Sn system. However the calculation remains flat over the whole C_b range in 4π (asterisks) and, even after filtering (circles), it gives a reasonably good reproduction of the data for $C_b >$ 1000 MeV.

The experimental standard deviation of the R_v distribution (rightmost panels) increases, as expected, with increasing centrality, probably due to the growth of the fluctuations in the nucleon-nucleon collision/exchange processes and in the secondary deexcitation. The standard deviation for the calculated events reproduces the trend of the experiments, although with a systematic underestimation. It is worth noting that the value of the standard deviation is found to be practically insensitive to y, t_{sw}, afterburner, and filtering.

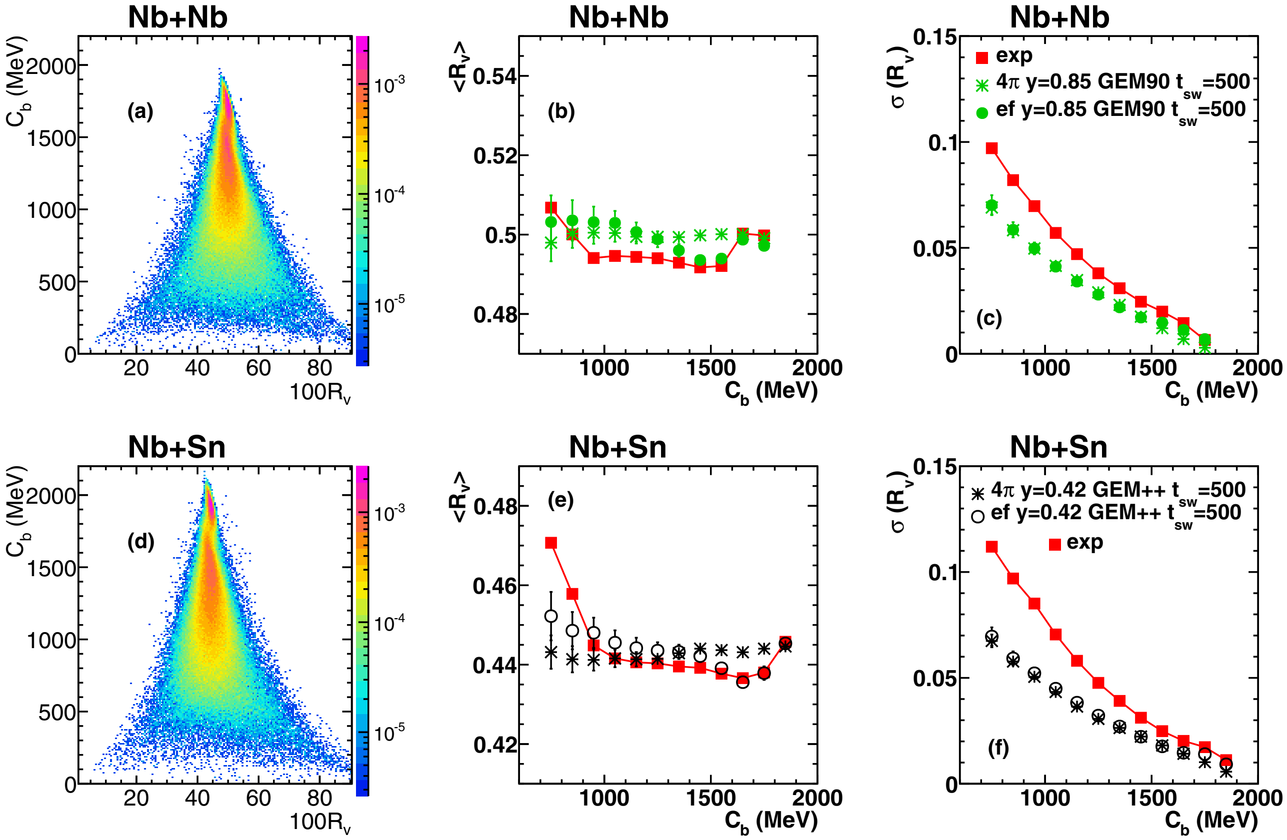

FIG. 4. Diffusion plot. Results of AMD plus GEMINI calculations for the reactions $^{93}\mathrm{Nb} + {}^{93}\mathrm{Nb}$ (upper panel) and $^{93}\mathrm{Nb} + {}^{116}\mathrm{Sn}$ (lower panels) at 38 MeV/nucleon. (a) Correlation ($100R_v$) vs. C_b with model parameters $y = 0.85$, $t_{\mathrm{sw}} = 500$ fm/c and GEM++; filtered results. (b) Mean of the R_v distribution vs. C_b. (c) Standard deviation of the R_v distribution vs. C_b. (d) Same as panel (a) but for $^{93}\mathrm{Nb} + {}^{116}\mathrm{Sn}$ with parameters $y = 0.42$, $t_{\mathrm{sw}} = 500$ fm/c and GEM++; filtered results. (e) Same as panel (b) but for $^{93}\mathrm{Nb} + {}^{116}\mathrm{Sn}$. (f) Same as panel (c) but for $^{93}\mathrm{Nb} + {}^{116}\mathrm{Sn}$. Full (red) squares are the experimental data. Other symbols are for calculated results; they refer to filtered events, except for asterisks, which are in 4π.

More calculations with a wider choice of the parameters were performed, but are not shown in Fig. 4 because their results do not differ very much from the presented ones and would just blur the picture.

In order to summarize with a single number the quality of the agreement between calculated results and experimental data for the mean value of a generic observable X, the average absolute percent deviation can be used,

$$Q_X = \frac{100}{N}\sum_{i=1}^{N}\frac{\left|\langle X\rangle_i^m - \langle X\rangle_i^e\right|}{\langle X\rangle_i^e}, \tag{5}$$

where $\langle X\rangle_i$ is the mean of the X distribution for model (apex m) and experiment (apex e) in the ith bin of the sorting variable (in our case C_b), and the summation index i runs over the chosen N bins. This indicator Q_X measures the goodness of the global agreement between experiment and calculations with different parameters: the smaller the indicator, the better the agreement. For the width of the X distribution one can use a similar indicator Σ_X, obtained from Eq. (5) by replacing $\langle X\rangle_i^e$ and $\langle X\rangle_i^m$ with $\langle\sigma(X)\rangle_i^e$ and $\langle\sigma(X)\rangle_i^m$, respectively.

The quality of the agreement between the experimental diffusion plot and those obtained with *all* the different calculations that were performed (varying y, t_{sw}, and afterburner) is presented in Table I,[5] by means of the above defined indicators, where the observable X is now R_v. A quick glance at the table shows that (i) the difference in $\langle R_v\rangle$ between experiment and calculations is always very small, around 0.8–1.0% (even in the asymmetric system where this outcome is not trivial); (ii) the calculations underestimate the standard deviations $\sigma(R_v)$ by about 30%; (iii) for the observable R_v, the calculations with different parameters do not substantially differ from each other.

The two-dimensional correlations between $\theta_{\mathrm{QP}}^{\mathrm{cm}}$ and C_b (Wilczynski plot) produced by the calculations are shown in Figs. 5(a) and 5(d) for filtered events from $^{93}\mathrm{Nb} + {}^{93}\mathrm{Nb}$ and $^{93}\mathrm{Nb} + {}^{116}\mathrm{Sn}$, respectively, with the same parameters used for Figs. 4(a) and 4(d). In the remaining panels of Fig. 5, the full (red) squares show, again as a function of C_b, the mean [(b) and (e)] and the standard deviation [(c) and (f)] of the $\theta_{\mathrm{QP}}^{\mathrm{cm}}$

---

[5] Here and in the following tables, the point with the largest C_b value is not used for calculating the indicators, because in the experiment it is strongly polluted by elastic events; the considered C_b range will be 700–1700 (700–1800) MeV for Nb+Nb (Nb+Sn).

TABLE I. Diffusion plot: indicators Q_R and Σ_R of the global percent deviations between experimental data and calculations (with different parameters y, t_{sw}, afterburner) for the mean and standard deviation, respectively, of the R_v distribution in the considered range of C_b (see text). The estimated statistical uncertainties are typically around 0.2% for Q_R and 1–2% for Σ_R.

		Nb + Nb										Nb + Sn			
	t_{sw} (fm/c) =	200		500		1000		2500		10000		200		500	
y	Evap-code	Q_R (%)	Σ_R (%)	Q_R (%)	Σ_R (%)	Q_R (%)	Σ_R (%)	Q_R (%)	Σ_R (%)	Q_R (%)	Σ_R (%)	Q_R (%)	Σ_R (%)	Q_R (%)	Σ_R (%)
0.85	GEM++	1.0	33	0.9	31	0.8	30	0.7	29	0.9	30				
	GEM90	0.9	30	0.9	28	0.7	27	0.7	27	0.9	28				
0.42	GEM++	1.0	31	0.9	31							1.0	31	1.0	32
	GEM90	0.9	28	0.9	26										

distributions for the two reactions. One observes the typical behavior of binary processes at intermediate energies: with decreasing C_b (i.e., with increasing centrality) the experimental average value of the polar angle first starts close to the grazing angle of very peripheral collisions, then approaches the beam axis and finally moves definitively away from it; at the same time the standard deviation increases monotonically, as expected on the basis of the growing importance of the fluctuations induced by nucleon-nucleon collisions and secondary decays. The other symbols are the results of some (out of several) calculations that were performed with different combinations of the parameters y, t_{sw} and afterburner. The effect

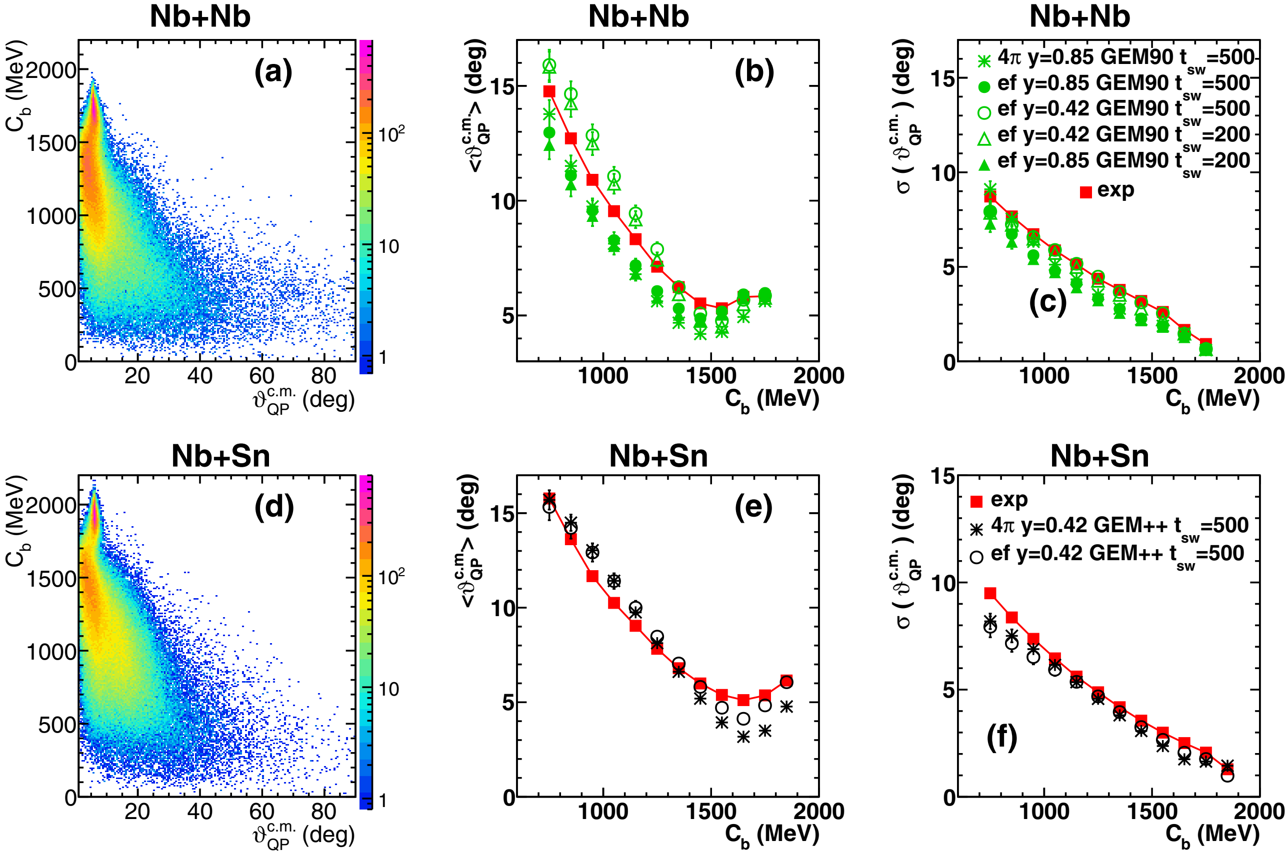

FIG. 5. Wilczynski plot. Results of AMD plus GEMINI calculations for the reactions ^{93}Nb + ^{93}Nb (upper panels) and ^{93}Nb + ^{116}Sn (lower panels) at 38 MeV/nucleon. (a) Correlation $\theta_{\mathrm{QP}}^{\mathrm{cm}}$ vs C_b with parameters $y = 0.85$, $t_{\mathrm{sw}} = 500$ fm/c and GEM++; filtered results. (b) Mean of the $\theta_{\mathrm{QP}}^{\mathrm{cm}}$ distribution vs C_b. (c) Standard deviation of the $\theta_{\mathrm{QP}}^{\mathrm{cm}}$ distribution vs C_b. (d) Same as panel (a) but for ^{93}Nb + ^{116}Sn with parameters $y = 0.42$, $t_{\mathrm{sw}} = 500$ fm/c and GEM++; filtered results. (e) Same as panel (b) but for ^{93}Nb + ^{116}Sn. (f) Same as panel (c) but for ^{93}Nb + ^{116}Sn. Full (red) squares are experimental data. Other symbols for calculated results; they refer to filtered events, except for asterisks, which are in 4π.

TABLE II. Wilczynski plot: indicators Q_θ and Σ_θ of the global percent deviations between experimental data and calculations (with different parameters y, t_{sw}, afterburner) for the mean and standard deviation, respectively, of the $\theta_{\mathrm{QP}}^{\mathrm{cm}}$ distribution in the considered range of C_b. The estimated statistical uncertainties are typically around 1–2% for both Q_θ and Σ_θ.

		Nb + Nb										Nb + Sn			
	t_{sw} (fm/c) =	200		500		1000		2500		10000		200		500	
y	Evap-code	Q_θ (%)	Σ_θ (%)	Q_θ (%)	Σ_θ (%)	Q_θ (%)	Σ_θ (%)	Q_θ (%)	Σ_θ (%)	Q_θ (%)	Σ_θ (%)	Q_θ (%)	Σ_θ (%)	Q_θ (%)	Σ_θ (%)
0.85	GEM++	18	30	15	26	12	21	11	21	12	20				
	GEM90	14	24	11	21	9	18	9	18	10	19				
0.42	GEM++	10	15	10	11							8	14	9	11
	GEM90	10	7	10	4										

of the experimental filter is again negligible. The calculations do a good job by reproducing very closely the behavior of the experimental data.

Focusing on the symmetric collision $^{93}\mathrm{Nb} + {}^{93}\mathrm{Nb}$, where calculations with two values of y were performed, one observes some sensitivity to a variation of the in-medium nucleon-nucleon cross section, although the results for the mean value of $\theta_{\mathrm{QP}}^{\mathrm{cm}}$ do not seem conclusive. A small improvement with $y = 0.42$ is observed for the standard deviation, but its interpretation is not clear. In any case, it will be shown in Sec. IV C that $y = 0.42$ gives a slightly worse reproduction of the chemistry of emitted LCPs and IMFs.

The obtained results for all performed calculations are summarized in Table II, where the deviations between experimental data and different simulations are shown in terms of the already defined indicators, evaluated for the observable $X \equiv \theta_{\mathrm{QP}}^{\mathrm{cm}}$. For the case $y = 0.85$ and with both GEMINI versions, one observes that the agreement with the experimental data first improves with increasing t_{sw} and then stabilizes. For example, with GEM++, Q_θ starts with 18% at $t_{\mathrm{sw}} = 200$ fm/c and then decreases to 15% and ∼12% for longer times. This is attributed to the already mentioned incomplete Coulomb deflection when the switching from AMD to GEMINI occurs too early. Using GEM90 brings a general, limited improvement, while the trend as a function of switching time remains the same. Also the Σ_θ indicator for the standard deviations displays the same behavior (slightly lower values with GEM90 and some improvement with larger t_{sw}), although its interpretation is not as obvious.

A further observable that can be investigated, although in a limited range of polar angles, is the charge $Z_{\mathrm{QP}}^{\mathrm{sec}}$ of the QP, detected by means of the silicon telescopes. The calculated two-dimensional correlations between $Z_{\mathrm{QP}}^{\mathrm{sec}}$ and C_b are shown in Figs. 6(a) and 6(d) for the reactions $^{93}\mathrm{Nb} + {}^{93}\mathrm{Nb}$ and $^{93}\mathrm{Nb} + {}^{116}\mathrm{Sn}$, respectively, with the same parameters used for Figs. 4(a) and 4(d). In the remaining panels of Fig. 6 the full (red) squares show, as a function of C_b, the mean [(b) and (e)] and the standard deviation [(c) and (f)] of the distribution of the experimental charge $Z_{\mathrm{QP}}^{\mathrm{sec}}$. The calculated results are shown with different symbols corresponding to different parametrizations. As expected, with increasing centrality of the collision, the mean of the $Z_{\mathrm{QP}}^{\mathrm{sec}}$ distribution steadily decreases, starting from the charge $Z = 41$ of the projectile in the most peripheral collisions, while the standard deviation increases. Figure 6 indicates that the agreement between experimental data and calculation is rather good for the means, while some systematic difference is present in the standard deviations.

As for the previous variables, Table III summarizes the deviation between the experimental data and all the calculated results by means of the quality indicators now applied to the observable $X \equiv Z_{\mathrm{QP}}^{\mathrm{sec}}$. There is a clear improvement when using GEM90 instead of GEM++. For example, for the calculation with $y = 0.85$ and $t_{\mathrm{sw}} = 200$ fm/c, the indicators Q_Z and Σ_Z decrease by about a factor of two. Focusing on the case $y = 0.85$ and GEM90, one observes an improvement when t_{sw} is increased from 200 to 500 fm/c, but longer times do not bring any further change. This suggests that the emissions of AMD between 200 and 500 fm/c differ from the emissions of GEMINI, but this difference becomes negligible beyond 500 fm/c. The charge of the QP shows little sensitivity to a reduction of the in-medium cross section from $y = 0.85$ to 0.42. However, with $y = 0.42$ the difference between 200 and 500 fm/c is reduced with respect to what happens with $y = 0.85$. This may be explained by the fact that lowering the in-medium cross section produces less nucleon-nucleon collisions and therefore attenuates the difference between dynamic and statistical emissions in the time interval between 200 and 500 fm/c.

C. Particle multiplicities

As a last point, the experimental total multiplicities of LCP ($Z = 1, 2$) and IMF ($Z = 3$–7) of Ref. [10], associated with two-body events from the reaction $^{93}\mathrm{Nb} + {}^{93}\mathrm{Nb}$, have been used for comparison with the total multiplicities obtained from AMD plus GEMINI calculations.[6]

Figure 7 displays the multiplicity of particles emitted in the forward c.m. hemisphere as a function of C_b, separately for the different species: protons in panel (a), deuterons in (b), tritons in (c), α particles in (d), IMF with $Z = 3$–7

---

[6] The separation between midvelocity and evaporative multiplicities is beyond the scope of this paper and will not be discussed.

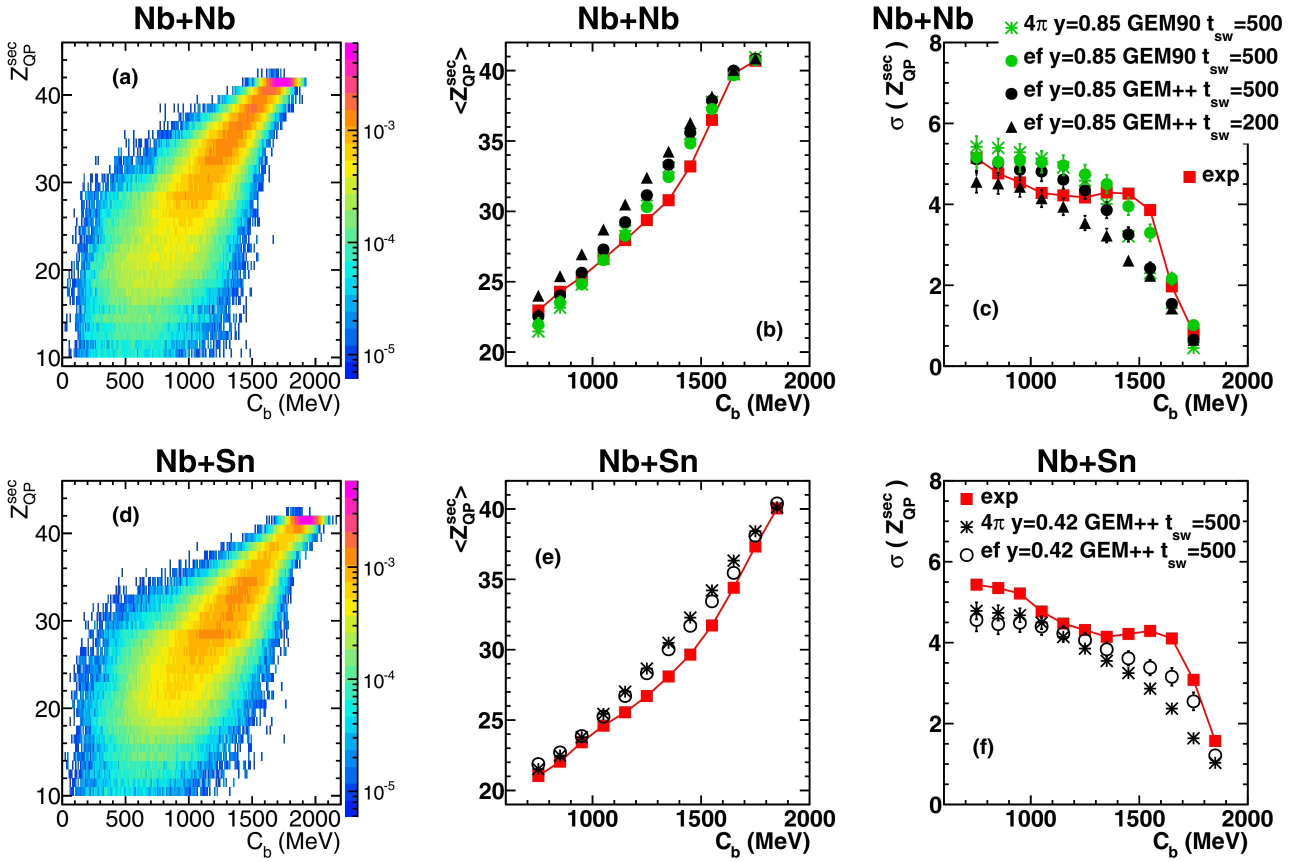

FIG. 6. Secondary charge of QP. AMD plus GEMINI calculations for the reactions ^{93}Nb + ^{93}Nb (upper panels) and ^{93}Nb + ^{116}Sn (lower panels) at 38 MeV/nucleon. (a) Correlation Z_{QP}^{sec} vs C_b, with $y = 0.85$, $t_{sw} = 500$ fm/c and GEM++; filtered results. (b) Mean of the Z_{QP}^{sec} distribution vs C_b. (c) Standard deviation of the Z_{QP}^{sec} distribution vs C_b. (d) Same as panel (a) but for the reaction ^{93}Nb + ^{116}Sn with $y = 0.42$, $t_{sw} = 500$ fm/c and GEM++; filtered results. (e) Same as panel (b) but for the reaction ^{93}Nb + ^{116}Sn. (f) Same as panel (c) but for the reaction ^{93}Nb + ^{116}Sn. Full (red) squares are experimental data of Ref. [29]. Other symbols are for calculated results; they refer to filtered events, except for asterisks, which are in 4π.

in (e). Both the experimental data [full (red) squares] from Fig. 3 of [10] and the calculated results with $t_{sw} = 500$ fm/c are presented. The circles represent the total multiplicities obtained by taking into account the emissions of the GEMINI afterburner, while the lines show the particles multiplicities produced by the dynamic code AMD, stopped at the indicated time t. With the exception of the protons (which are always overestimated by the calculations) and to a minor extent of the IMFs, the remaining experimental multiplicities are quite well reproduced by the AMD model with $y = 0.85$, coupled with GEM90 [full (green) circles]. In fact, with the GEM90 afterburner one observes a clear improvement with respect to GEM++ (full black circles) even for protons, because their calculated multiplicity is strongly reduced and approaches the

TABLE III. Z_{QP} vs C_b correlation: indicators Q_Z and Σ_Z of the global percent deviations between experimental data and calculations (with different parameters y, t_{sw}, afterburner) for the mean and standard deviation, respectively, of the Z_{QP} distribution in the considered range of C_b. Estimated statistical uncertainties are typically around 0.4% for Q_Z and 2% for Σ_Z.

		Nb + Nb										Nb + Sn			
	t_{sw} (fm/c) =	200		500		1000		2500		10000		200		500	
y	Evap-code	Q_Z (%)	Σ_Z (%)	Q_Z (%)	Σ_Z (%)	Q_Z (%)	Σ_Z (%)	Q_Z (%)	Σ_Z (%)	Q_Z (%)	Σ_Z (%)	Q_Z (%)	Σ_Z (%)	Q_Z (%)	Σ_Z (%)
0.85	GEM++	6.8	18	3.7	13	3.3	12	3.2	11	3.5	14				
	GEM90	4.3	9	2.7	10	2.9	12	2.7	12	2.6	11				
0.42	GEM++	6.5	14	4.6	12							7.1	17	4.2	14
	GEM90	3.6	9	1.9	8										

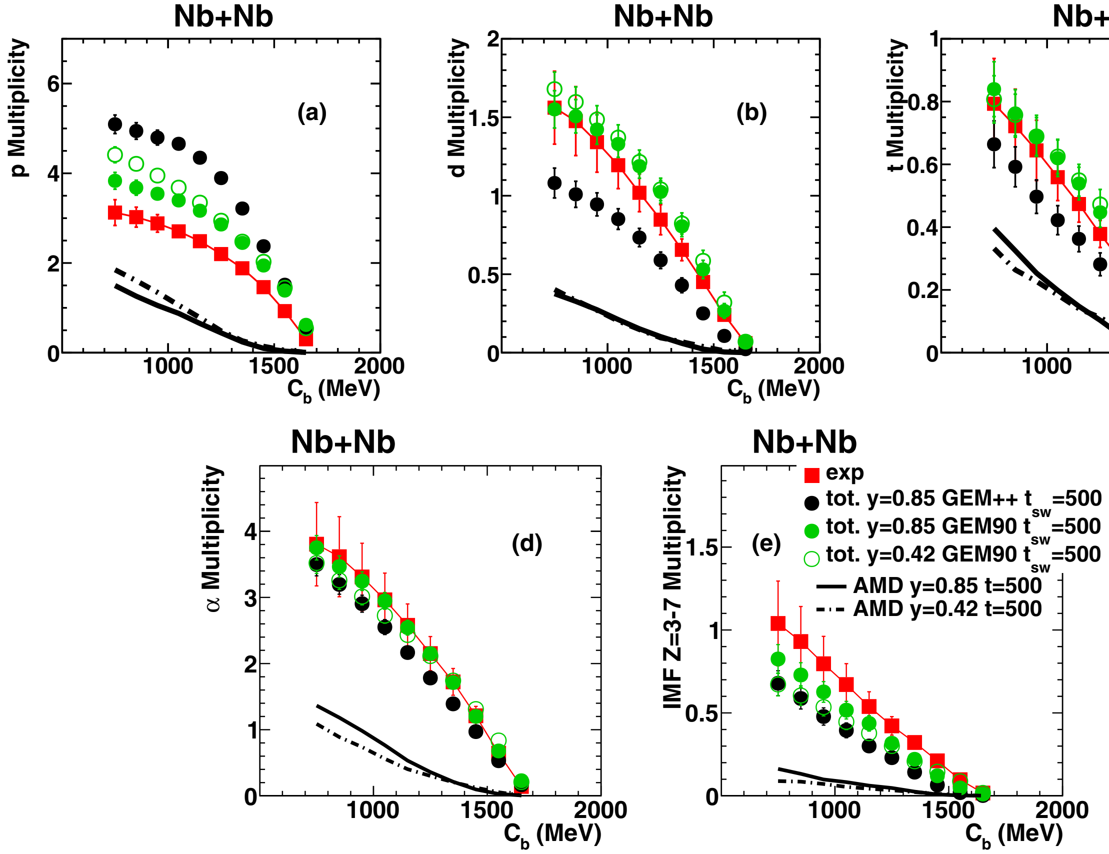

FIG. 7. Multiplicities of LCPs and IMFs ($Z = 3$–7), forward emitted in the c.m. frame, as a function of C_b for the system ^{93}Nb + ^{93}Nb at 38 MeV/nucleon: (a) protons, (b) deuterons, (c) tritons, (d) α particles, and (e) IMF ($Z = 3$–7). Experimental data of Ref. [10] [full (red) squares] are compared with the results of calculations, all with $t_{\rm sw} = 500$ fm/c, but different y (0.85 or 0.42) or afterburner (GEM90 or GEM++). Circles correspond to AMD plus GEMINI (GEM++ in black, GEM90 in green), lines to results of AMD alone, stopped at the indicated time t.

experimental data from above. A relevant difference between GEM90 and GEM++ lies in the adopted expression for the level density, which is that of Ref. [24] for GEM++ and that of Ref. [44] for GEM90. In fact, it was verified that if the level density parametrization of GEM90 is implemented in GEM++, the difference between the results of the two versions is strongly reduced. A possible explanation of the better agreement with GEM90 may be due to the fact that GEM++ was optimized so as to reproduce experimental data for rather heavy nuclei (mainly in the range $A \approx 100$–200 [24]), while the decaying QP of Ref. [10] are likely to have masses in the range $A \approx 40$–93.

As mentioned in Sec. IV B, the decrease of y from 0.85 (full green circles) to 0.42 (open green circles) tends to slightly worsen the quality of the agreement between calculated results and experimental data, mainly for less peripheral collisions and especially for protons and α particles. Another point worth noting is that a sizable amount of particles are directly produced by AMD (lines). Of course, such a contribution, which is produced with a dynamic formalism, originates partly during the interaction of the colliding nuclei, but partly also after their reseparation.

The evolution of the multiplicities for protons, deuterons, and α particles when the switching times increase from 200 up to 10 000 fm/c is presented in Fig. 8. The upper panels refer to GEM90, the lower ones to GEM++. Again, the lines are the multiplicities from AMD without afterburner, obtained with the standard value $y = 0.85$ for the in-medium cross section. They show a general increase from 200 fm/c (dashed lines) to 500 fm/c (full lines) and 2500 fm/c (dotted lines), while a further delay of $t_{\rm sw}$ up to 10 000 fm/c (dash-dotted lines) does not produce any appreciable effect, with the notable exception of protons. Another point worth noting is that, at $t_{\rm sw} = 10\,000$ fm/c, the protons produced by the AMD alone in the less peripheral collisions already reach the experimental data, therefore the addition of the evaporative emissions with whatever GEMINI version leads to an overestimation of the data. Thus, at very long times, AMD seems to have some problems, which are put in particular evidence by the very large production of protons.

With AMD plus GEM90 (upper panels), the total multiplicities of α particles and IMFs (not shown) are almost independent of switching times, as one would expect for a good matching of the two models. However, this does not happen for protons and deuterons, which display opposite trends with switching time: when $t_{\rm sw}$ increases, the total multiplicity of protons increases too (reaching an overestimation of the experimental data of about 50%), while that of deuterons decreases (leading to an underestimation of about 50% at long times). This means that in the time interval between 200 and

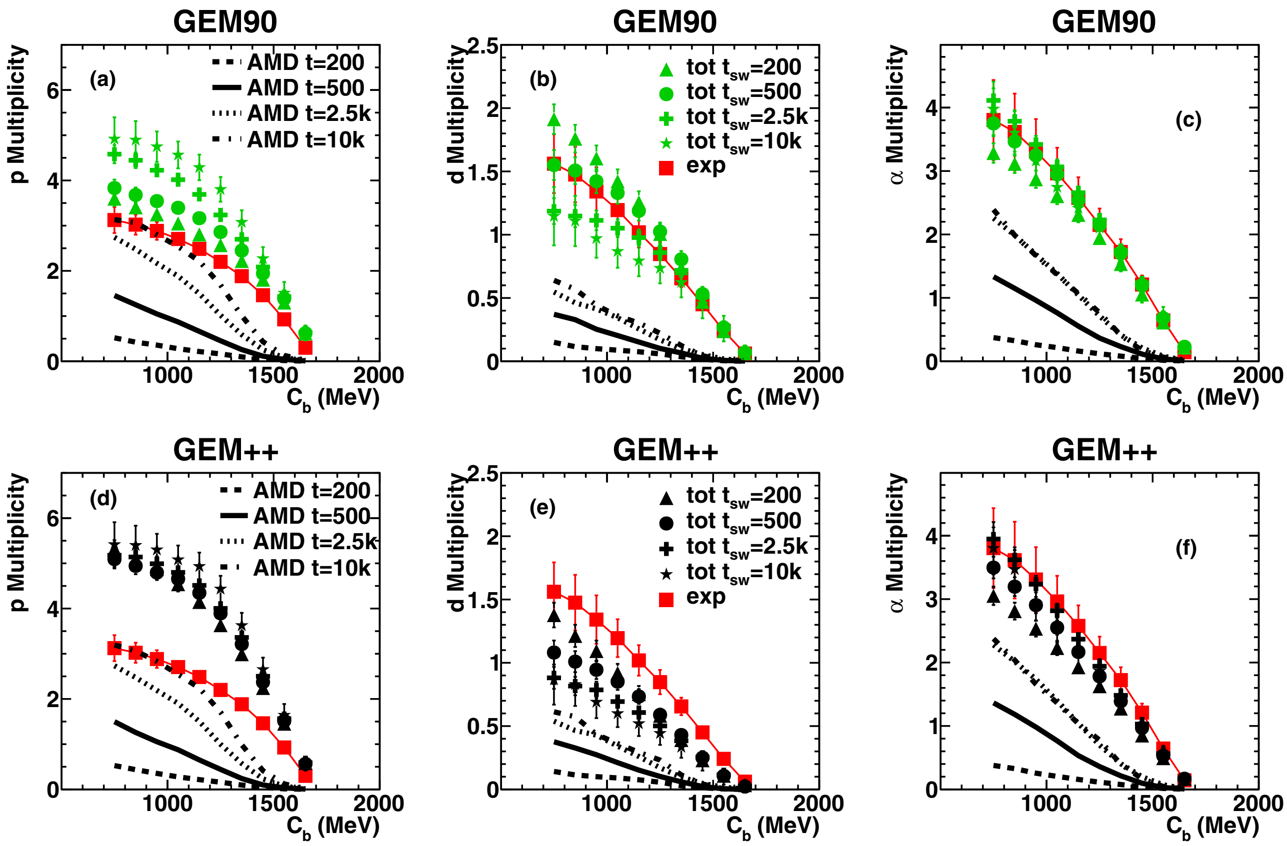

FIG. 8. Multiplicities of LCPs, forward emitted in the c.m. frame, as a function of C_b for the system ^{93}Nb + ^{93}Nb at 38 MeV/nucleon: (a), (d) protons; (b), (e) deuterons; (c), (f) α particles. Experimental data [full (red) squares] are compared with results of calculations with $y = 0.85$ and different values of t_{sw} (in fm/c). Symbols correspond to AMD plus GEMINI (GEM90 in upper panels, GEM++ in lower ones), black lines to results of AMD alone, stopped at the indicated time t.

10 000 fm/c AMD tends to produce more protons (and less deuterons) than GEM90, while the two codes produce similar amounts of more complex particles.

The total multiplicities of the various particles obtained with AMD plus GEM++ (symbols in the lower panels) appear to be much less dependent on switching times: the case of protons, where all symbols are practically superposed, is especially striking, and also the results for the deuterons are less spread out than with GEM90. This may be an indication that the particle production of AMD at long times resembles more the evaporation described by GEM++ than that by GEM90. However the results with GEM++ present a much worse agreement with the data: at all switching times the multiplicity of deuterons underestimates the experimental data and that of the protons overestimates them by a good factor of 2.

All results concerning the global deviations (indicator Q_M) of the calculated particle multiplicities from the experimental values of Ref. [10] are presented in Table IV for different values of the calculation parameters. The entries of this table confirm that, using GEM90, the deviations from the experimental values are sizably reduced for all particles and practically at all switching times. For tritons and α particles Q_M becomes comparable to or even smaller than its estimated uncertainty, thus indicating a very good agreement between model and experiment, within errors. Thus, for the particle multiplicities, the calculation that best reproduces all experimental data seems to be AMD coupled with the GEM90 afterburner, with a switching time of about 500 fm/c and a preference for $y = 0.85$.

Figure 9 presents the total charge of LCPs plus IMFs ($Z = 3$–7), forward emitted in the c.m. frame of the colliding system, obtained by adding the charges of the particles weighted with their respective multiplicities. First of all, it is worth noting the good agreement, for almost all choices of parameters, of the calculated total charge Z_{emitted} with the measured one, which is again represented by the full (red) squares that are hardly visible below the symbols of the various calculations. The two versions of GEMINI [GEM++ in (a) and GEM90 in (b)] reproduce equally well the total emitted charge, although they give a different chemistry of the emitted particles (see Fig. 7). Second, the calculated Z_{emitted} is practically independent of the switching time of the dynamic calculation, with the possible exception of $t_{\text{sw}} = 200$ fm/c (triangles), for which the total emitted charge is somewhat underestimated. As already noted about Table III, this may be an indication of dynamic effects between 200 and 500 fm/c. In fact the calculations somewhat overestimate the final charge $Z_{\text{QP}}^{\text{sec}}$ of the QP and underestimate by the same amount the total charge of LCPs and IMFs in such a way that they still sum up to $Z \approx 41$. Third, the use of $y = 0.42$ slightly reduces the total

TABLE IV. Multiplicities of LCPs and IMFs ($Z = 3$–7) in the reaction ^{93}Nb + ^{93}Nb at 38 MeV/nucleon: indicators Q_M of the average percent deviation between experimental data of Ref. [10] and calculated multiplicities (with different parameters y, t_{sw}, afterburner, and stiff/soft equation of state) in the considered range of C_b. Typical estimated statistical uncertainties on Q_M are of the order of 4–8%.

		t_{sw} (fm/c) :	200	500		2500	10000
		asy-EoS :	stiff	stiff	soft	stiff	stiff
LCP	y	Evap-code	Q_M (%)	Q_M (%)	Q_M (%)	Q_M (%)	Q_M (%)
p	0.85	GEM++	64	68	64	74	86
		GEM90	18	29	24	47	64
	0.42	GEM++	64	80			
		GEM90	20	39			
d	0.85	GEM++	30	35	19	43	49
		GEM90	16	12	28	13	17
	0.42	GEM++	30	31			
		GEM90	16	19			
t	0.85	GEM++	33	30	23	27	28
		GEM90	8	10	16	6	12
	0.42	GEM++	29	25			
		GEM90	11	16			
α	0.85	GEM++	24	15	22	8	13
		GEM90	11	2	6	4	5
	0.42	GEM++	23	17			
		GEM90	11	9			
IMF	0.85	GEM++	62	50	53	53	50
		GEM90	40	28	33	42	44
	0.42	GEM++	60	56			
		GEM90	32	30			

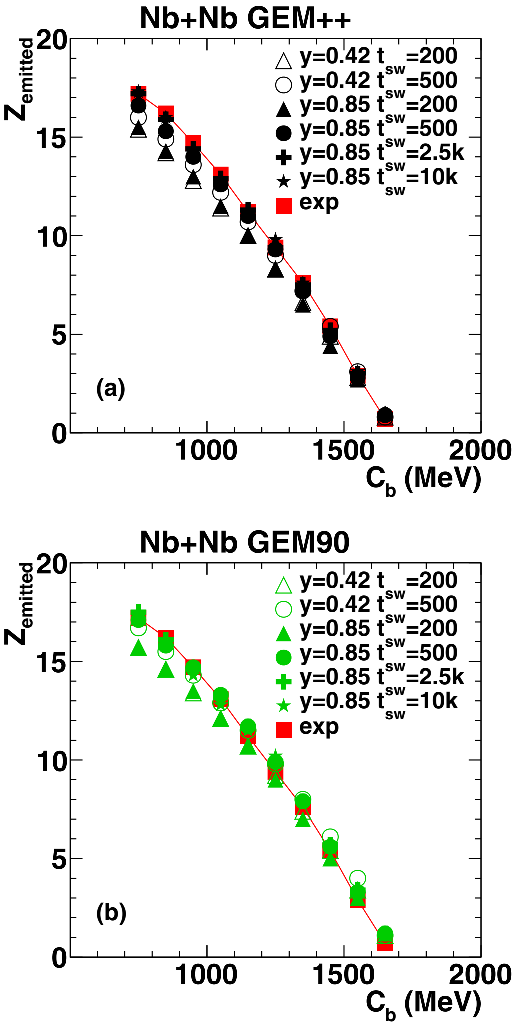

FIG. 9. Total charge of all LCPs and IMFs ($Z = 3$–7) forward emitted in the c.m. reference frame of the collision for the ^{93}Nb + ^{93}Nb reaction. Full (red) squares represent experimental data, the other symbols results of various calculations with GEM++ (upper) and GEM90 (lower) afterburner. Switching times are in units of fm/c.

emitted charge (open symbols compared with full symbols) in the less peripheral collisions, and this again may be attributed to a reduced importance of dynamic effects at short times and to lower dissipation of kinetic energy, resulting in less excited nuclei.

A last point to be addressed is the isospin dependence of the equation of state. The isospin degree of freedom plays an important role in determining the exit channels. In fact isospin transport phenomena, related to the isospin gradient between target and projectile (isospin diffusion [45,46]) or to the density gradient between QP-QT (which are both at normal density) and the more diluted midvelocity zone (isospin drift [46]) have been observed in several experiments (see, e.g., Refs. [47–54]). Of course, some sensitivity to the effects of an asy-stiff or asy-soft interaction in the AMD calculations may be expected only for mass-resolved light particles. Figure 10 shows the results with AMD only (lines) or with AMD plus GEMINI afterburner (symbols), for the two hypotheses about the equation of state mentioned at the beginning of Sec. III. The panels show again results for protons [(a) and (d)], deuterons [(b) and (e)], and α particles [(c) and (f)], with GEM90 (upper panels) and GEM++ (lower panels), and experimental values again represented by full (red) squares.

In the dynamic calculations without afterburner, protons and α particles present a very small difference between the asy-stiff (full lines) and asy-soft (dashed lines) interaction, and this insensitivity remains also after the GEMINI decay. Apparently, there is a remarkable signal for deuterons, which are produced more abundantly (by a factor of about 2) with the asy-soft equation of state, as found also in Ref. [22]. Actually this effect, which at first sight might seem to favor an asy-soft AMD plus GEM++, is very likely to be an artifact. Its explanation resides in the fact that, when the soft SLy4 force [33] is used in the present version of AMD, one finds that it largely overestimates the deuteron binding energy. In contrast, the stiff parametrization gives a deuteron binding energy much closer to the true value and it also reproduces rather well the measured deuteron multiplicities with GEM90.

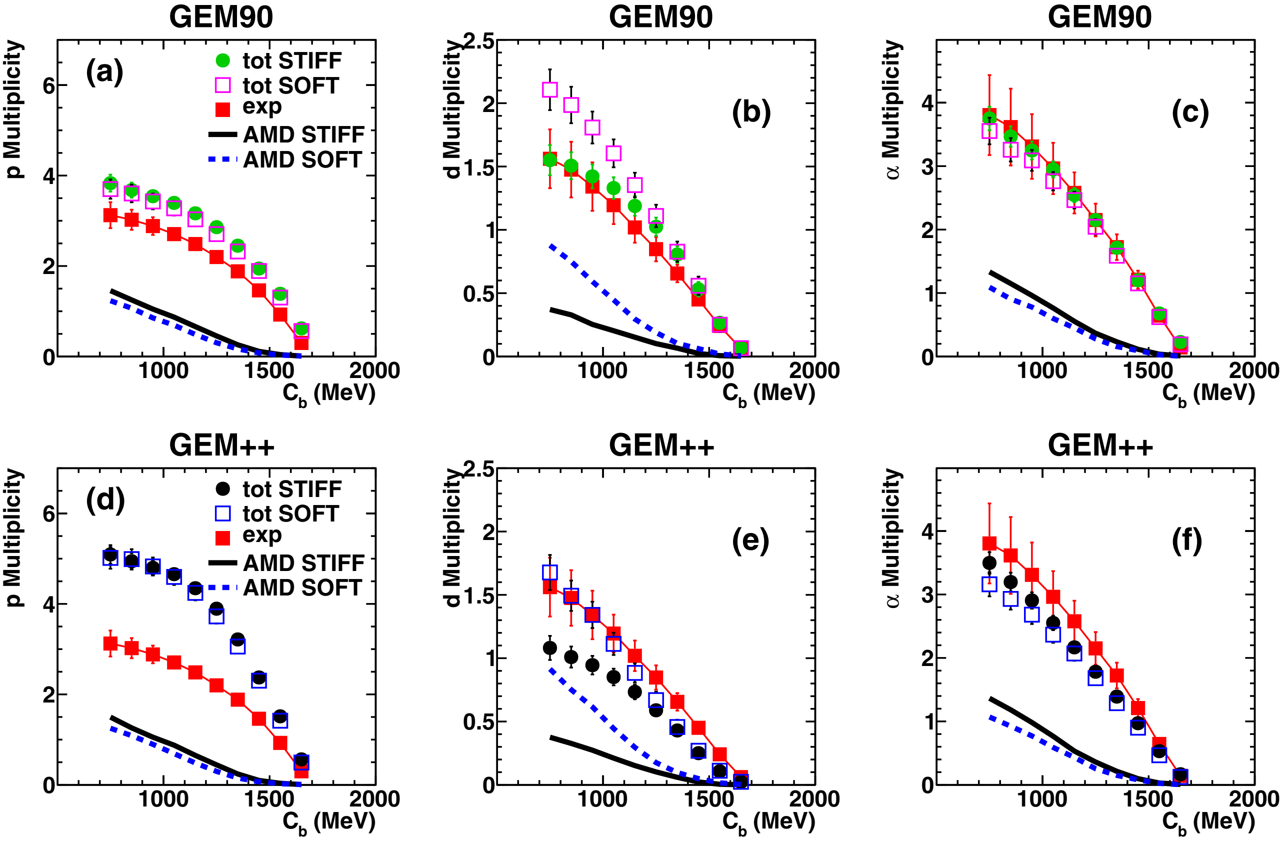

FIG. 10. Same as Fig. 8, but here experimental data [full (red) squares] are compared with calculations ($y = 0.85$ and $t_{sw} = 500$ fm/c) performed with an asy-stiff and an asy-soft version of the equation of state in the AMD model. Lines (symbols) correspond to results of AMD without (with) afterburner. The asy-stiff results are those of Fig. 8, presented with the same lines/symbols and colors. Upper panels refer to GEM90, lower panels to GEM++.

V. SUMMARY AND CONCLUSIONS

In this work the properties of quasiprojectiles (QP) detected in peripheral and semiperipheral collisions of the reactions ^{93}Nb + ^{93}Nb and ^{93}Nb + ^{116}Sn at 38 MeV/nucleon have been compared with calculations performed with the dynamic code AMD, followed by the statistical code GEMINI (GEM++ and GEM90) as an afterburner.

In the literature one can find other papers [21–23] in which the results of the AMD model are compared with existing experimental data, but they usually focus on central collisions and on the properties of IMFs produced in light systems. Those papers have shown that AMD is able to reproduce in a very good way many characteristics of such reactions. The comparison presented in this paper demonstrates, for the first time to our knowledge, the capability of the AMD-plus-GEMINI calculations to reproduce also characteristic features of peripheral and semiperipheral collisions in the Fermi energy regime, where (quasi)binary collisions still exhaust a major part of the reaction cross section.

Experimental data and calculated results were sorted in bins of centrality by means of an observable, C_b, which is built from the secondary velocities of QP and QT. A good reproduction of the average velocity ratio R_v and of the QP secondary charge Z_{QP}^{sec} was obtained in the calculations, with little sensitivity to the screening parameter y for the nucleon-nucleon in-medium cross section. The QP c.m. polar angle θ_{QP}^{cm} shows some dependence on y, which, however, does not allow one to draw definite conclusions about which value has to be preferred.

Concerning the switching time t_{sw} from the dynamic code AMD to the GEMINI afterburner, the present analysis indicates that for the observables related to the QP properties (R_v, θ_{QP}^{cm}, Z_{QP}) there is an improvement when t_{sw} is extended at least to 500 fm/c.

The comparison between experimental data and calculations was performed also for the total multiplicities of light charged particles and IMFs ($Z = 3$–7) of Ref. [10]. It was found that the chemistry of these particles is strongly dependent on the afterburner version that is used (GEM90 or GEM++), probably because of the different level density parametrizations in the two versions of the code. In fact, for a given AMD calculation, the experimental multiplicities are better reproduced with the GEM90 afterburner. Concerning the in-medium nucleon-nucleon cross section, there is no compelling evidence that the standard screening parameter $y = 0.85$ needs to be changed in semiperipheral collisions. The obtained agreement, although not perfect, is reasonably acceptable for all particles, except protons, which are always overestimated by the calculations. However, things are not completely satisfactory and there are still unclear points concerning the evaporation of the GEMINI afterburner and its matching with the dynamic code AMD.

The calculated particle multiplicities seem generally insensitive to the stiffness of the adopted isospin-dependent part of the equation of state. The remarkable sensitivity of the deuteron multiplicity is most likely an artifact due to the wrong deuteron binding energy produced by the effective force parametrized for an asy-soft equation of state.

In conclusion, the AMD-plus-GEMINI calculations proved to be a reliable tool for describing heavy ion collisions in the Fermi energy regime, not only for central collisions (as already shown in the literature), but also for peripheral and semiperipheral ones.

ACKNOWLEDGMENTS

One of the authors (A. Ono) acknowledges the support from INFN - Sezione di Firenze for his stay in 2017, and the support from Japan Society for the Promotion of Science KAKENHI Grants No. 17K05432 and No. 24105008. This work required the use of a lot of computation time for the production of the simulated data. We would like to thank the GARR Consortium for the kind use of the cloud computing infrastructure on the platform cloud.garr.it. We would like to thank also the CNAF center of INFN for the use of its cloud computing infrastructure.

[1] V. Baran, M. Colonna, and M. D. Toro, Nucl. Phys. A **730**, 329 (2004).

[2] D. R. Bowman, G. F. Peaslee, N. Carlin, R. T. de Souza, C. K. Gelbke, W. G. Gong, Y. D. Kim, M. A. Lisa, W. G. Lynch, L. Phair *et al.*, Phys. Rev. Lett. **70**, 3534 (1993).

[3] C. P. Montoya, W. G. Lynch, D. R. Bowman, G. F. Peaslee, N. Carlin, R. T. de Souza, C. K. Gelbke, W. G. Gong, Y. D. Kim, M. A. Lisa *et al.*, Phys. Rev. Lett. **73**, 3070 (1994).

[4] J. Tõke, B. Lott, S. P. Baldwin, B. M. Quednau, W. U. Schröder, L. G. Sobotka, J. Barreto, R. J. Charity, D. G. Sarantites, D. W. Stracener, and R. T. de Souza, Phys. Rev. Lett. **75**, 2920 (1995).

[5] J. Dempsey, R. Charity, L. Sobotka, G. Kunde, S. Gaff, C. K. Gelbke, T. Glasmacher, M. J. Huang, R. C. Lemmon, W. G. Lynch *et al.*, Phys. Rev. C **54**, 1710 (1996).

[6] J. Tõke, D. K. Agnihotri, S. P. Baldwin, B. Djerroud, B. Lott, B. M. Quednau, W. Skulski, W. U. Schröder, L. G. Sobotka, R. J. Charity, D. G. Sarantites, and R. T. de Souza, Phys. Rev. Lett. **77**, 3514 (1996).

[7] J. Łukasik, J. Benlliure, V. Métivier, E. Plagnol, B. Tamain, M. Assenard, G. Auger, C. O. Bacri, E. Bisquer, B. Borderie, R. Bougault *et al.*, Phys. Rev. C **55**, 1906 (1997).

[8] E. Plagnol, J. Łukasik, G. Auger, C. O. Bacri, N. Bellaize, F. Bocage, B. Borderie, R. Bougault, R. Brou, P. Buchet *et al.* (The INDRA Collaboration), Phys. Rev. C **61**, 014606 (1999).

[9] S. Piantelli, L. Bidini, G. Poggi, M. Bini, G. Casini, P. R. Maurenzig, A. Olmi, G. Pasquali, A. A. Stefanini, and N. Taccetti, Phys. Rev. Lett. **88**, 052701 (2002).

[10] S. Piantelli, P. R. Maurenzig, A. Olmi, L. Bardelli, A. Bartoli, M. Bini, G. Casini, C. Coppi, A. Mangiarotti, G. Pasquali, G. Poggi, A. A. Stefanini, N. Taccetti, and E. Vanzi, Phys. Rev. C **74**, 034609 (2006).

[11] J. Lecolley, D. Durand, M. Aboufirassi, R. Bougault, J. Colin, A. Genoux-Lubain, C. L. Brun, O. Lopez, M. Louvel, C. Meslin, G. Rudolf, L. Stuttgge, and S. Tomasevic, Phys. Lett. B **387**, 460 (1996).

[12] N. Marie, R. Laforest, R. Bougault, J. P. Wieleczko, D. Durand, Ch. O. Bacri, J. F. Lecolley, F. Saint-Laurent, G. Auger, J. Benlliure, E. Bisquer, B. Borderie *et al.*, Phys. Lett. B **391**, 15 (1997).

[13] M. D'Agostino, P. Mastinu, P. Milazzo, M. Bruno, D. Bowman, P. Buttazzo, L. Celano, N. Colonna, J. Dinius, A. Ferrero *et al.*, Phys. Lett. B **368**, 259 (1996).

[14] J. Frankland, C. Bacri, B. Borderie, M. Rivet, M. Squalli, G. Auger, N. Bellaize, F. Bocage, R. Bougault, R. Brou *et al.*, Nucl. Phys. A **689**, 905 (2001).

[15] J. Frankland, B. Borderie, M. Colonna, M. Rivet, C. Bacri, P. Chomaz, D. Durand, A. Guarnera, M. Parlog, M. Squalli *et al.*, Nucl. Phys. A **689**, 940 (2001).

[16] M. Colonna, M. Di Toro, A. Guarnera, S. Maccarone, M. Zielinska-Pfabe, and H. H. Wolter, Nucl. Phys. A **642**, 449 (1998).

[17] P. Napolitani and M. Colonna, Phys. Lett. B **726**, 382 (2013).

[18] Y.-X. Zhang, Y.-J. Wang, M. Colonna, P. Danielewicz, A. Ono, M. B. Tsang, H. Wolter, Jun Xu, L.-W. Chen, D. Cozma *et al.*, Phys. Rev. C **97**, 034625 (2018).

[19] J. Xu, L.-W. Chen, M. Tsang, H. Wolter, Y.-X. Zhang, J. Aichelin, M. Colonna, D. Cozma, P. Danielewicz, Z.-Q. Feng *et al.*, Phys. Rev. C **93**, 044609 (2016).

[20] A. Ono, H. Horiuchi, T. Maruyama, and A. Ohnishi, Phys. Rev. Lett. **68**, 2898 (1992).

[21] A. Ono, S. Hudan, A. Chbihi, and J. D. Frankland, Phys. Rev. C **66**, 014603 (2002).

[22] A. Ono, J. Phys.: Conf. Ser. **420**, 012103 (2013).

[23] G. Tian, Z. Chen, R. Han, F. Shi, F. Luo, Q. Sun, L. Song, X. Zhang, G. Q. Xiao, R. Wada, and A. Ono, Phys. Rev. C **97**, 034610 (2018).

[24] R. J. Charity, Phys. Rev. C **82**, 014610 (2010).

[25] R. J. Charity, M. McMahan, G. Wozniak, R. McDonald, L. Moretto, D. Sarantites, L. Sobotka, G. Guarino, A. Pantaleo, L. Fiore, A. Gobbi, and K. Hildenbrand, Nucl. Phys. A **483**, 371 (1988).

[26] R. Charity, K. Jing, D. Bowman, M. McMahan, G. Wozniak, L. Moretto, N. Colonna, G. Guarino, A. Pantaleo, L. Fiore, A. Gobbi, and K. Hildenbrand, Nucl. Phys. A **511**, 59 (1990).

[27] A. Mangiarotti, P. R. Maurenzig, A. Olmi, S. Piantelli, L. Bardelli, A. Bartoli, M. Bini, G. Casini, C. Coppi, A. Gobbi, G. Pasquali, G. Poggi, A. A. Stefanini, N. Taccetti, and E. Vanzi, Phys. Rev. Lett. **93**, 232701 (2004).

[28] S. Piantelli, P. R. Maurenzig, A. Olmi, L. Bardelli, M. Bini, G. Casini, A. Mangiarotti, G. Pasquali, G. Poggi, and A. A. Stefanini, Phys. Rev. C **76**, 061601(R) (2007).

[29] S. Piantelli, A. Mangiarotti, P. R. Maurenzig, A. Olmi, L. Bardelli, M. Bini, G. Casini, G. Pasquali, G. Poggi, and A. A. Stefanini, Phys. Rev. C **78**, 064605 (2008).

[30] M. Bini, G. Casini, A. Olmi, G. Poggi, A. A. Stefanini, L. Bardelli, A. Bartoli, L. Bidini, C. Coppi, P. Del Carmine, A. Mangiarotti, P. R. Maurenzig, G. Pasquali, S. Piantelli, S. Poggi, N. Taccetti, and E. Vanzi, Nucl. Instrum. Methods A **515**, 497 (2003).

[31] A. Ono, Phys. Rev. C **59**, 853 (1999).

[32] N. Ikeno, A. Ono, Y. Nara, and A. Ohnishi, Phys. Rev. C **93**, 044612 (2016).

[33] E. Chabanat, P. Bonche, P. Haensel, J. Meyer, and R. Schaeffer, Nucl. Phys. A **635**, 231 (1998).

[34] A. Ono, H. Horiuchi, T. Maruyama, and A. Ohnishi, Prog. Theor. Phys. **87**, 1185 (1992).

[35] A. Ono and H. Horiuchi, Phys. Rev. C **53**, 845 (1996).

[36] D. D. S. Coupland, W. G. Lynch, M. B. Tsang, P. Danielewicz, and Y. Zhang, Phys. Rev. C **84**, 054603 (2011).

[37] O. Lopez, D. Durand, G. Lehaut, B. Borderie, J. D. Frankland, M. F. Rivet, R. Bougault, A. Chbihi, E. Galichet, D. Guinet *et al.* (INDRA Collaboration), Phys. Rev. C **90**, 064602 (2014).

[38] M. Wang, G. Audi, A. H. Wapstra, F. G. Kondev, M. MacCormick, X. Xu, and B. Pfeiffer, Chin. Phys. C **36**, 1603 (2012).

[39] https://wustl.app.box.com/s/ehsih9oc1j41loxgl4ox.

[40] G. Casini, P. Maurenzig, A. Olmi, and A. Stefanini, Nucl. Instrum. Methods A **277**, 445 (1989).

[41] J. Lukasik and Z. Majka, Acta Phys. Pol. B **24**, 1959 (1993).

[42] G. Casini, P. R. Maurenzig, A. Olmi, M. Bini, S. Calamai, F. Meucci, G. Pasquali, G. Poggi, A. A. Stefanini, A. Gobbi, and K. D. Hildenbrand, Phys. Rev. Lett. **78**, 828 (1997).

[43] G. Casini, M. Bini, S. Calamai, R. Laforest, P. R. Maurenzig, A. Olmi, G. Pasquali, S. Piantelli, G. Poggi, F. Saint-Laurent, J. C. Steckmeyer, A. A. Stefanini, and N. Taccetti, Eur. Phys. J. A **9**, 491 (2000).

[44] B. J. Fineman, K.-T. Brinkmann, A. L. Caraley, N. Gan, R. L. McGrath, and J. Velkovska, Phys. Rev. C **50**, 1991 (1994).

[45] M. Di Toro, V. Baran, M. Colonna, and V. Greco, J. Phys. G **37**, 083101 (2010).

[46] V. Baran, M. Colonna, V. Greco, and M. Di Toro, Phys. Rep. **410**, 335 (2005).

[47] M. B. Tsang, T. X. Liu, L. Shi, P. Danielewicz, C. K. Gelbke, X. D. Liu, W. G. Lynch, W. P. Tan, G. Verde, A. Wagner *et al.*, Phys. Rev. Lett. **92**, 062701 (2004).

[48] M. B. Tsang, Y. Zhang, P. Danielewicz, M. Famiano, Z. Li, W. G. Lynch, and A. W. Steiner, Phys. Rev. Lett. **102**, 122701 (2009).

[49] I. Lombardo, C. Agodi, R. Alba, F. Amorini, A. Anzalone, I. Berceanu, G. Cardella, S. Cavallaro, M. B. Chatterjee, E. De Filippo *et al.*, Phys. Rev. C **82**, 014608 (2010).

[50] E. De Filippo, A. Pagano, P. Russotto, F. Amorini, A. Anzalone, L. Auditore, V. Baran, I. Berceanu, B. Borderie, R. Bougault *et al.*, Phys. Rev. C **86**, 014610 (2012).

[51] S. Barlini, S. Piantelli, G. Casini, P. R. Maurenzig, A. Olmi, M. Bini, S. Carboni, G. Pasquali, G. Poggi, A. A. Stefanini *et al.* (FAZIA Collaboration), Phys. Rev. C **87**, 054607 (2013).

[52] S. Piantelli, S. Valdré, S. Barlini, G. Casini, M. Colonna, G. Baiocco, M. Bini, M. Bruno, A. Camaiani, S. Carboni *et al.*, Phys. Rev. C **96**, 034622 (2017).

[53] A. Jedele, A. B. McIntosh, K. Hagel, M. Huang, L. Heilborn, Z. Kohley, L. W. May, E. McCleskey, M. Youngs, A. Zarrella, and S. J. Yennello, Phys. Rev. Lett. **118**, 062501 (2017).

[54] A. Rodriguez Manso, A. B. McIntosh, A. Jedele, K. Hagel, L. Heilborn, Z. Kohley, L. W. May, A. Zarrella, and S. J. Yennello, Phys. Rev. C **95**, 044604 (2017).